# Unlocking electrostrain in plastically deformed barium titanate

*Fangping Zhuo,* Bo Wang, Long Cheng, Edoardo Zatterin, Tianshu Jiang, Fan Ni, Patrick Breckner, Yan Li, Nicolas Guiblin, Daniel Isaia, Nengneng Luo, Lovro Fulanović, Leopoldo Molina-Luna, Brahim Dkhil, Long-Qing Chen, and Jürgen Rödel**

F. Zhuo, F. Ni, P. Breckner, L. Fulanović, D. Isaia, J. Rödel

Department of Materials and Earth Sciences, Technical University of Darmstadt, 64287 Darmstadt, Germany

E-mail: zhuo@ceramics.tu-darmstadt.de; roedel@ceramics.tu-darmstadt.de

B. Wang

Materials Science Division, Lawrence Livermore National Laboratory, Livermore, USA

L. Cheng, N. Guiblin, B. Dkhil

Université Paris-Saclay, CentraleSupélec, CNRS, Laboratoire SPMS, 91190 Gif-sur-Yvette, France

E. Zatterin

ESRF, The European Synchrotron71 Avenue des Martyrs, Grenoble 38000, France

T. Jiang, L. Molina-Luna

Advanced Electron Microscopy Division, Department of Materials and Earth Sciences, Technical University of Darmstadt, 64287 Darmstadt, Germany

Y. Li

Department of Mechanical Science and Bioengineering, Osaka University, Osaka 560-8531, Japan

N. Luo

Center on Nanoenergy Research, State Key Laboratory of Featured Metal Materials and Life-cycle Safety for Composite Structures; School of Resources, Environment and Materials; Guangxi University, 530004 Nanning, China

L.-Q. Chen

Materials Research Institute and Department of Materials Science and Engineering, The Pennsylvania State University, University Park, PA 16802, USA

Achieving substantial electrostrain alongside a large effective piezoelectric strain coefficient ($d_{33}$*) in piezoelectric materials remains a formidable challenge for advanced actuator applications. Here, we propose a straightforward approach to enhance these properties by strategically designing the domain structure and controlling the domain switching through the

introduction of arrays of ordered {100}<100> dislocations. This dislocation engineering yields an intrinsic lock-in steady-state electrostrain of 0.69% at a low field of 10 kV $cm^{-1}$ without external stress and an output strain energy density of 5.24 J $cm^{-3}$ in single-crystal $BaTiO_3$, outperforming the benchmark piezoceramics and relaxor ferroelectric single-crystals. Additionally, applying a compression stress of 6 MPa fully unlocks electrostrains exceeding 1%, yielding a remarkable $d_{33}$* value over 10000 pm $V^{-1}$ and achieving a record-high strain energy density of 11.34 J $cm^{-3}$. We employ optical and transmission electron microscopy, paired with laboratory and synchrotron X-ray diffraction, to rationalize the observed electrostrain. Phase-field simulations further elucidate the impact of charged dislocations on domain nucleation and domain switching. Our findings present an effective and sustainable strategy for developing high-performance, lead-free piezoelectric materials without the need for additional chemical elements, offering immense potential for actuator technologies.

Keywords: plastic deformation, ordered dislocations, strain, piezoelectric actuator

## 1. Introduction

Piezoelectric actuators, converting electrical energy into mechanical displacement, serve a variety of applications including micro/nanopositioning systems, optical equipment, micro robot dynamic systems and motors, where the electric-field-induced strain (electrostrain) is a critical performance indicator.[1–3] A notable development was the discovery of a substantial strain of 1.7% (driving electric field of ~120 kV $cm^{-1}$) in lead-based relaxor ferroelectric single crystals.[4] This breakthrough, coupled with environmental regulations against the use of toxic lead, has sparked a race over the past two decades to develop lead-free piezoceramics with electrostrain exceeding 1%.[5–8] Despite their piezoelectric properties being comparable to commercially used $Pb(Zr,Ti)O_3$ (PZT)-based ceramics (common driving electric field of 20 kV $cm^{-1}$), the requirement for higher driving electric fields remains a significant obstacle to their broader application as actuators. Consequently, the effective piezoelectric strain coefficient

($d_{33}$*), often falls below that of state-of-the-art lead-based single crystals (~2500 pm $V^{-1}$).[4] The challenge of achieving large electrostrains at low fields in lead-free ceramics persists, driven by the escalating demand for consumer electronics and the imperative of miniaturization,[9] spurring the ongoing quest for high-performance and environmentally-friendly piezoelectric materials. Piezoelectric ceramics and crystals remain the preferred materials for actuator applications, largely due to their superior mechanical energy densities. A high mechanical energy density, represented as $U_m = (1/2)YS^2$ (where $Y$ is Young's modulus and $S$ is the actuation strain), is essential for actuator materials to generate sufficient force to drive loads effectively.[9]

In recent years, various strategies have emerged to improve intrinsic and extrinsic electrostrain responses. For example, constructing morphotropic/polymorphic phase boundary (MPB/PPB)[8,10] and texturing[11] are common approaches to enhance the intrinsic piezoelectric strain related to polarization extension and rotation,[12,13] albeit typically limited to 0.1% in magnitude. Extrinsic contributions to piezoelectric strain may arise from few mechanisms, including field-induced phase transitions,[14] flexoelectricity-induced breaking of centrosymmetry,[15] local structural heterogeneity,[16] non-180° domain switching,[17] interactions between defects and polarization switching,[18,19] migration of charged point defects,[20] and electrobending deformation.[21,22] For instance, introduction of point defects, such as oxygen vacancies, into a lattice typically forms defect dipoles that can be oriented through aging, acting as a strong restoring force and leading to non-180° domain switching, thereby demonstrating a large electrostrain (0.75%) in Fe-doped $BaTiO_3$ crystals.[17] Over the past three years, high electric field-induced strains exceeding 1% have been reported in the $Bi_{0.5}Na_{0.5}TiO_3$ (BNT)-based ceramics (driven by 100 kV $cm^{-1}$)[23,24] and (K, Na)$NbO_3$ (KNN)-based ceramics (driven by 50 kV $cm^{-1}$).[18] More recently, a high-record $d_{33}$* of 3500 pm $V^{-1}$ with an ultrahigh electrostrain of 0.7% at a reduced field of 20 kV $cm^{-1}$ was reported in

$(K_{0.48}Na_{0.52})_{0.99}NbO_{2.995}$ ceramics by defect dipole stretching design.[25] Nevertheless, some of the mechanisms described above require complex compositions and chemical elements, atmosphere-assisted sintering, and poling-aging treatments that can take hours or even days. Therefore, there is a pressing need for lead-free piezoceramics with simple compositions, easy processing, and high electrostrain performance.

Dislocations, one-dimensional (1D) defects in crystalline materials, are often considered a nuisance because they can frequently degrade a material's electrical properties.[26] In oxide ceramics, dislocations can carry both a strain singularity and a compensating charge zone around them.[27] Ferroelectric materials present an ideal platform for investigating dislocation-tuned functionality in ceramics, as they exhibit a strong coupling between lattice and charge degrees of freedom.[28] For example, we demonstrated that extrinsic contributions to piezoelectric strain from the dislocation-domain wall interactions can be an order of magnitude higher than intrinsic ones, leading to the emergence of large $d_{33}$* in single-crystal $BaTiO_3$ at a low field of 0.5 kV $cm^{-1}$.[28–31] However, the resultant electrostrain is about 0.01% in magnitude due to the principally limited local domain switching caused by dislocation-domain wall interactions. Recently, local control of ferroelectric domain switching was attempted in a marginally twisted $WS_2$ bilayer by introducing dislocations networks.[32] These attempts highlight new opportunities for attaining both high electrostrain and substantial $d_{33}$*, in which unprecedented electrostrain properties might be enabled with fewer chemical elements by tailoring domains and domain switching at different length scales.

Our strategy is implemented by utilizing irreversible plastic deformation of barium titanate lead-free model ferroelectric single crystals, which imprints {100}<100> dislocation system with the Burgers vector [100]. It therefore provides a means of 1D doping as it does not require any additional elements.[33] Introducing arrays of ordered dislocations into single-crystal

$BaTiO_3$ inhibits the formation of out-of-plane ferroelectric domain variants defined by the [001] plane, which was confirmed by transmission electron microscopy and scanning x-ray diffraction microscopy. An intrinsic steady-state strain of 0.69% at room temperature is manifested in the deformed samples without external stress. We also demonstrate the attainment of a high reversible electrostrain of 1.03%, approaching the theoretical limit of tetragonality (the ratio of out-of-plane to in-plane unit cell parameters, *c/a*) of barium titanate, with an ultrahigh $d_{33}$* value bigger than 10000 pm $V^{-1}$ at room temperature under a low field of 10 kV $cm^{-1}$. The intrinsic lock-in and ultrahigh electrostrains are attributed to the electric-field-induced domain switching between out-of-plane and in-plane domains (defined by [100]/[010] domain wall).

## 2. Results and Discussion

Metals and alloys are typically malleable and ductile due to metallic bonding, whereas most oxide ceramics are brittle due to strong iono-covalent bonding that causes repulsive interactions when atoms slide past each other, resulting in undesirable dislocations and limited plastic deformability.[34] Despite the presence of limited number of available slip systems for activation, dislocations can nevertheless be imprinted in some single crystal oxides with considerable precision.[28,30,31,35] To introduce a high density of aligned dislocations, $BaTiO_3$ single crystals were plastically deformed by uniaxial compression along the [110] crystallographic direction with a strain rate of $10^{-5}$ $s^{-1}$ at 1150 °C, see Methods and Figure S1, Supporting Information. Comparing optical images taken before and after deformation, the macroscopic effect of the mechanical imprint is evident in the altered domain structures (**Figure** 1a,b). Loading along the [110] direction activates the {100}<100> slip systems (see schematic in Figure 1c), featuring a forest of dislocations with a line vector of $\zeta$ = [001] (Figure 1d). Our previous results revealed that these {100}<100> dislocation fields promote the nucleation of ferroelectric domains with spontaneous polarizations oriented within the [100]/[010] plane in $BaTiO_3$.[28] This may lead to

the formation of stripe domain structures with walls parallel to the sample edges, as schematically illustrated in Figure 1e.

In the deformed samples, pure edge dislocations are predominant and distributed inhomogeneously, appearing as points when viewed on the (001) plane, see transmission electron microscopy (TEM) image in Figure 1f. The stress-strain curve (Figure S1, Supporting Information) had little increase in stress after the yield point (no obvious strain hardening). Such a curve usually corresponds to the easy gliding of a single slip system, without much interaction between deformation-induced dislocations. The edge-type and perfectly aligned dislocation arrangement confirmed that dislocation glide is the underlying mechanism for plastic deformability.[36] The dislocation density is estimated to be $2.0\times10^{12}$ $m^{-2}$ by quantifying the viewed dislocations on the (001) plane from several TEM images, corresponding to an average spacing of 700 nm. The average dislocation spacing ($L$) was determined using a standard approximation $\rho = 1/L^2$, where $\rho$ is the dislocation density. This dislocation density matches well with our previously reported values.[30,31] Notably, the domain walls are oriented parallel or perpendicular to the [110] crystallographic direction, suggesting the formation of in-plane $a_1$ and $a_2$ domains with polarization vectors oriented along the [100] and [010] directions, respectively. The high-angle annular dark-field scanning TEM (HAADF-STEM) image revealed a Burgers vector of a[100] (see the Burgers circuit around the dislocation in Figure 1g), where a is the lattice parameter. Dislocation glide is accompanied by displacement of both Ba and Ti layers, resulting in a Ti-rich dislocation core (Figure S2, Supporting Information). Lattice rotation mapping derived from Geometric Phase Analysis (GPA, see methods) displays the typical dislocation-associated strain fields (see strain field $\varepsilon_{xx}$ in Figure 1h; $\varepsilon_{xy}$ and $\varepsilon_{yy}$ in Figure S3, Supporting Information). The a[100] edge-dislocation core in $SrTiO_3$ has been experimentally confirmed to be charged;[37] however, the quantitative mapping of space charges and oxygen vacancies near the charged dislocation cores in $BaTiO_3$ is beyond the scope of this

study. Such analysis demands continuous efforts and relies on electron microscopy techniques like electron-energy-loss spectroscopy.[38]

Synchrotron-based scanning X-ray diffraction microscopy (SXDM) is a non-destructive scanning probe technique that allows to image lattice deformations with a spatial resolution of tens of nanometers.[39–41] A sketch illustrating the working principle of SXDM is provided in Figure S3, Supporting Information. In this work, SXDM was used to collect a raster scan of three-dimensional reciprocal space maps (3D-RSMs) around the (033) Bragg condition within a selected area of the deformed sample (Figure S4, Supporting Information). The result of this scan is a five-dimensional (5D) dataset consisting of scattered intensity $I$ as a function of the two direct space sample coordinates ($x$, $y$) that make up the scanned area, and the three reciprocal space coordinates ($q_x$, $q_y$, $q_z$) defining the volume probed by each 3D-RSM, i.e. $I(x, y, q_x, q_y, q_z)$. Integrating this dataset along ($x$, $y$) yields the average 3D-RSM over the probed area, whose $q_z$ projection is depicted in Figure 1i. This plot reveals the presence of four distinct (033) Bragg peaks, each stemming from the four different possible domain variants ($a_1^+$, $a_1^-$, $a_2^+$, $a_2^-$) of in-plane $a$ domains (Figure 1j). Computing the centre of mass of $I(q_x, q_y, q_z)$ at each ($x$, $y$) position allows to obtain an image of these domains as the map of angular distances of the local $\boldsymbol{q}_{033}$ vector at ($x$, $y$) if the (033) peak in the cubic paraelectric phase (Figure 1k) is quantified. In Figure 1l, this computation was repeated for a sub-volume of reciprocal space containing only the peaks of the blue and green $a_1$ domains, enabling the identification of regions of strong local lattice tilts in the vicinity of domain walls, i.e., dislocations.[39] The average spacing between dislocations is estimated to be about 2 μm, which aligns well with the value obtained by TEM.

The dislocation-induced nucleation of in-plane $a$ domains was further documented by taking optical images from different areas of the sample (Figure S5, Supporting Information), which

is in good agreement with our design strategy (Figure 1e). The reference undeformed samples favored both *a*/*c* and $a_1/a_2$ 90° domain walls on the (001) plane, documented in optical microscope images (Figure S6, Supporting Information). The *c* domains are characterized by spontaneous polarization vectors aligned parallel to the [001] direction. Our mechanical dislocation imprint provides therefore a strategic method to selectively manipulate polarizations, enabling control over the domain structure of bulk ferroelectric crystals.[28,29] This strategy may open up new possibilities for developing a foundation for dislocation-tuned domain formation and switching in ferroelectric materials, enabling the customization of their properties to suit specific application needs.

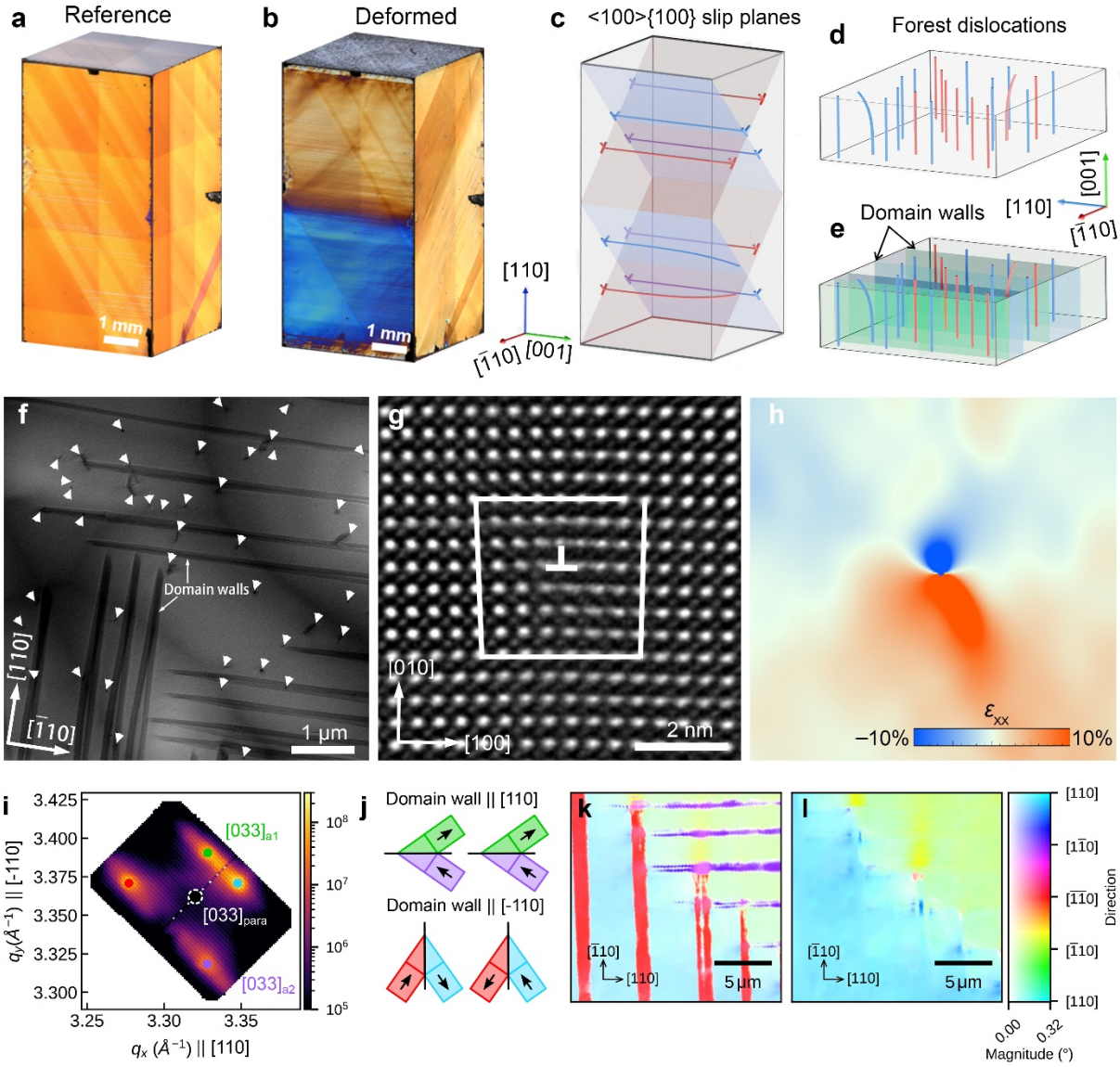

**Fig. 1.** a, b) Typical domain arrangement for a tetragonal [110]-oriented $BaTiO_3$ single crystal imaged with differential interference contrast before and after deformation. c) Schematic illustration of the high-temperature {100}<100> slip systems activated during uniaxial compressive plastic deformation. d) The [001]-sliced samples have well-aligned dislocations oriented in the [001] direction and e) have the nucleation of in-plane domains. f) A representative bright-field TEM image for the deformed sample viewing on the (001) plane. g) HAADF-STEM image featuring an edge dislocation with Burgers vector $\boldsymbol{b}$ = a[100], and h) the corresponding in-plane strain ($\varepsilon_{xx}$) map calculated by using GPA. i) $q_z$ projection of the average 3D-RSM collected around the (033) Bragg condition. The four different possible domain variants are marked with distinct colors. j) Schematics illustrating the formation of domain walls parallel to the [110] and [$\bar{1}$10] directions with domain variants corresponding to the four distinct (033) Bragg peaks in (i). k) SXDM map of the angular tilt of $q$-vectors normal to (033) lattice planes, with different colors indicating the presence of four tetragonal ferroelectric domains. l) The same map in (k), but focusing on local $q$-vector deviations from the average of two of the four domains, highlighting regions of localized lattice deformations near the domain walls, i.e., dislocations.

The introduced mesoscopic dislocation structure had a significant impact on polarization response, such as reduced maximum polarization ($P_m$), remanent polarization ($P_r$) and enhanced coercive field (**Figure 2**a). A 4-fold increase in the back-switching process ($P_{back} = P_m - P_r$) was quantified, and the polarization did not reach saturation, suggesting dislocation-induced domain wall pinning.[29] The reference sample exhibited a symmetric butterfly-like strain loop, while the deformed sample featured a highly asymmetric bipolar strain curve (see first and second cycles in Figure 2b). The asymmetric appearance of the strain loops revealed in Figure 2b is suggested to be due to the presence of a strong internal bias originating from imprinted dislocations in the deformed samples.[29,42] The asymmetric strain loops are influenced by the interplay between dislocations and domain walls, which can lead to a polarization offset.[43] This offset primarily affects the strain response but has a minimal impact on the overall polarization loop, which remains largely symmetric. Specifically, the original domain structure after plastic deformation was locked-in by the dislocations but could be unlocked by a modest electric field. It is suggested that the specific dislocation density of $2.0 \times 10^{12}$ $m^{-2}$ allows to specify the strength of the dislocation lock. The room temperature electrostrain in positive electric field was greatly enhanced, reaching a maximum value of over 1% (Figure 2b). The

maximum electrostrain at room temperature is approaching the 1.1% difference in the lattice parameter of $BaTiO_3$.[44] However, after the electric field was removed, intrinsic lock-in strain of 0.36% was observed (Figure 2c), indicating a remnant degree of irreversible switching between in-plane *a*-domains and out-of-plane *c*-domains. A steady-state maximum strain of 0.69% along with a $d_{33}$* of 6900 pm $V^{-1}$ was unlocked after multiple unipolar loading up to 100 cycles (Figure 2c and Figure S7, Supporting Information), which is much higher than the electrostrains in the state-of-the-art relaxor ferroelectric single crystals $Pb(Mg_{1/3}Nb_{2/3})O_3$-$PbTiO_3$ (PMN-PT) and commercially used $Pb(Zr,Ti)O_3$ (PZT) ceramics under the same field of 10 kV $cm^{-1}$ (see unipolar strain curves in Figure 2c). Our method achieved improved temperature stability of electrostrain values at the first and tenth unipolar cycles when compared with those reported in literature (Figure 2d and detailed unipolar strain loops in Figures S8 and S9, Supporting Information). Note that the $K_{0.43}Na_{0.57}NbO_3$ single crystals exhibit an unprecedented and temperature-sensitive $d_{33}$* values of above 9000 pm $V^{-1}$ at an electric field of 5 kV $cm^{-1}$.[52] Our obtained steady-state strain exhibits minimal sensitivity to frequency changes in the range of 0.01 Hz to 100 Hz, as displayed in Fig. S10 in the Supporting Information. In our case, the contribution of bending deformation to the overall strain in our samples is minimal and can be reasonably neglected, particularly for a 1 mm thick single crystal. In our geometry, a possibly bending deformation is not pertinent as can be verified using beam theory.

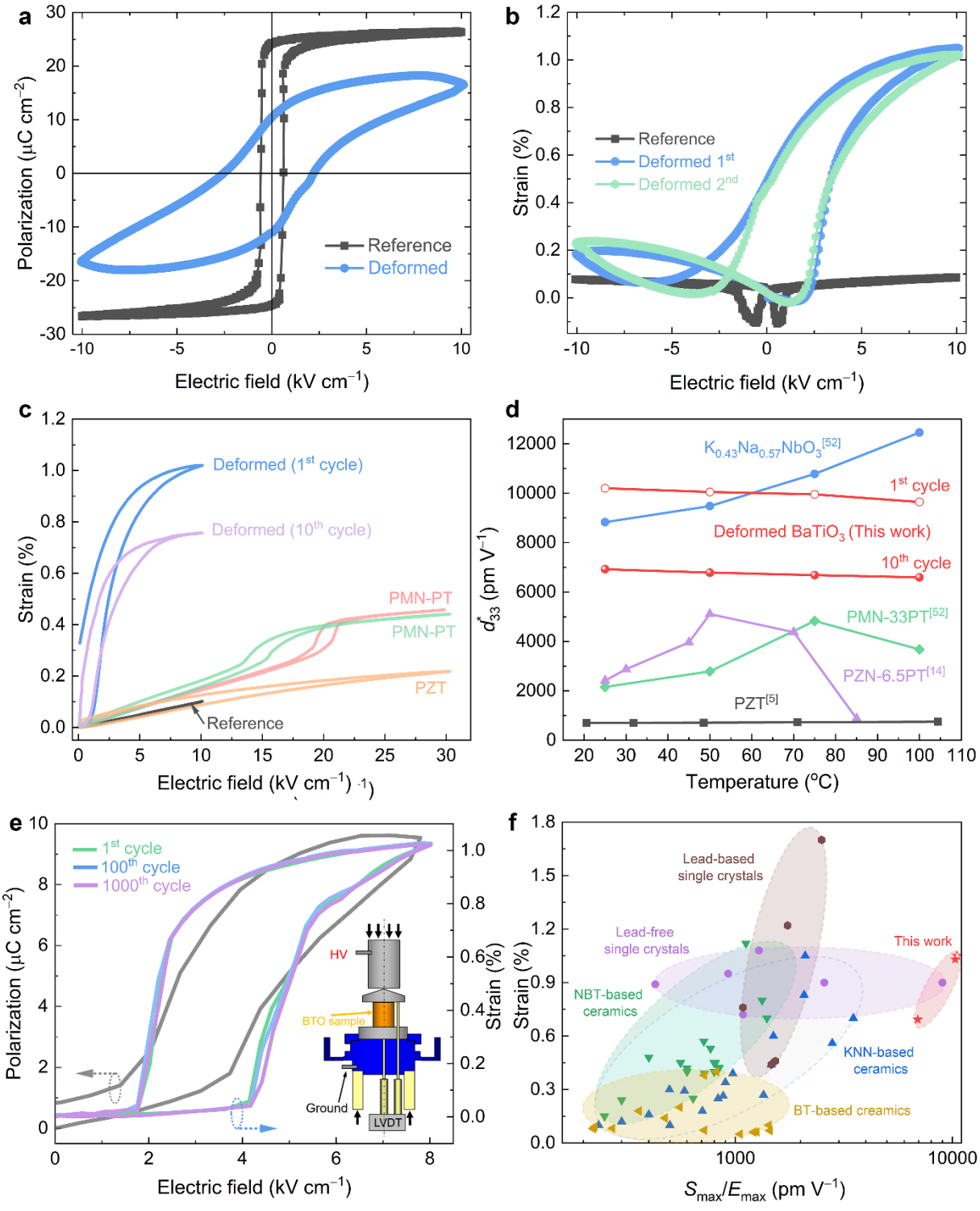


**Fig. 2.** a) Room-temperature polarization–electric field (*P*–*E*) loops and b) strain–electric field (*S*–*E*) curves of the deformed and undeformed reference samples measured at 1 Hz. c) Comparison of unipolar strains among piezoelectric materials. d) Comparison of temperature-dependent large-signal piezoelectric coefficient $d_{33}$* values with those reported in literature. PMN-33PT refers to $0.67Pb(Mg_{1/3}Nb_{2/3})O_3$-$0.33PbTiO_3$ single crystals and PZN-6.5PT means $0.935Pb(Zn_{1/3}Nb_{2/3})O_3$-$0.065PbTiO_3$ single crystals. The unipolar measurement was performed along the [001] pseudo-cubic direction at a frequency of 1 Hz. e) Room-temperature polarization loop and strain loops of the deformed sample measured at 1 Hz and under a

compressive stress of 6 MPa applied along the [001] direction. The inset highlights the Linear Variable Differential Transformer (LVDT) system for precise strain measurements. f) Comparison of room temperature electrostrains reported for state-of-the-art lead-based and lead-free piezoelectric materials. The open symbol indicates the data obtained from the first cycle unipolar strain loop.

Our measurements of dielectric permittivity and the corresponding direct piezoelectric coefficient ($d_{33}$) suggested that a short aging treatment of about 30 min at room temperature can switch all induced *c* domains back to *a* domains after removing the electric field (Figure S11, Supporting Information). This *c*-to-*a* domain back switching was also locally confirmed by using piezoresponse force microscopy (PFM), as featured by the changes in the color contrast of the out-of-plane phase images in Figure S12, Supporting Information. Note that high electrostrains of 0.9% were observed in $BaTiO_3$ single crystals when a critical compressive stress of 2 MPa was utilized.[45] Therefore, applying a small compressive stress would be sufficient to fully unlock the actuation strains in the deformed samples. We demonstrated that a compressive stress of 6 MPa facilitates the reversible switching between *a*- and *c*-domains, achieving a substantial electrostrain of 1.03% and nearly complete back-switching with a $P_r$ value of 1 μC $cm^{-2}$ (Figure 2e). Remarkably, these large actuation strains remain stable even after 1000 electric field cycles. As plotted in Figure 2e, under a pre-stress of 6 MPa, the actuation strain curve of the deformed crystal at the 1000th cycle mirrors that of the first cycle. A comparison of electrostrain performance of the deformed samples with representative piezoelectrics is provided in Figure 2f, where deformed single-crystal $BaTiO_3$ is superior to the lead-free piezoceramics[2,5,6,18,23,25,46–52] and even comparable with those of both lead-free and lead-based single crystals.[4,17,49–53] The required operating electric field is below 10 kV $cm^{-1}$, resulting in a large-signal piezoelectric coefficient ($d_{33}$*) of >10000 pm $V^{-1}$. In Table 1, we compare the deformed $BaTiO_3$ single crystals with a range of materials noted for their high strain responses,[4,54–57] including the poly(vinylidene fluoride) (PVDF)-based ferroelectric polymers and nanocomposites, $Pb(Zn_{1/3}Nb_{2/3})O_3$-$PbTiO_3$ (PZN-PT) relaxor ferroelectric single

crystals and PZT ceramics. The volumetric strain energy density (known as the output mechanical energy density), also crucial in evaluating an actuator material,[58] is proportional to $YS_m^2/2$, where $Y$ is the Young's modulus, $S_m$ represents the maximum strain level. Remarkably, the deformed $BaTiO_3$ single crystal with its large actuation strain and high modulus (220 GPa; Supplementary Figure S13, Supporting Information), enables the output of a record strain energy density of 11.67 J cm$^{-3}$. This is over 30 times greater than that of ferroelectric polymers[55,56] and an order of magnitude higher than those of piezoelectric ceramics and relaxor ferroelectric single crystals,[4,57] and comparable to PVDF/$TiO_2$ ferroelectric polymer nanocomposites.[54] The obtained strain energy density in this work is more than three orders of magnitude higher than our previous reported values,[28–31] where we applied very small subcoercive fields and observed only minimal displacements and strains. Therefore, our mechanical imprinting engineering strategy introduces 1D dislocations, and enables excellent actuation strain and volumetric strain energy density in single-crystal $BaTiO_3$ without necessitating complex electromechanical loading[61] and special treatments such as long time aging,[17] which could be very useful in actuator devices.

Table 1 Comparison of the strain and strain energy density for various material systems.

| Sample | $Y$ [GPa] | $S_m$ [%] | $YS_m^2/2$ [J cm$^{-3}$] | Ref. |
|---|---|---|---|---|
| PVDF/$TiO_2$ nanocomposites | 3.46 | 8.1 | 11.32 | [54] |
| irradiated P(VDF-TrFE)[a)] | 0.38 | 4.0 | 0.30 | [55] |
| P(VDF-TrFE-CTFE)[b)] | 0.40 | 4.0 | 0.32 | [56] |
| Piezoceramic (PZT-4) | 64 | 0.10 | 0.13 | [57] |
| PZN-PT single crystal | 7.7 | 1.70 | 1.11 | [4] |
| Deformed $BaTiO_3$[c)] | 200[d)] | 0.02 | 0.004 | [29] |

| | | | | |
|---|---|---|---|---|
| Reference | 209[d)] | 0.1 | 0.10 | This work |
| Deformed sample | 220 | 0.69[e)] | 5.24 | This work |
| Deformed sample | 220 | 1.03[f)] | 11.67 | This work |

[a)]TrFE refers to trifluoroethylene. [b)]CTFE denotes chlorotrifluoroethylene. [c)]Sample was deformed by uniaxial compression along the [001] direction. [d)]The data were obtained by nanoindentation experiments.[59,60] [e)]The steady-state strain value without compressive stress and [f)]The steady-state strain value under a compressive stress of 6 MPa.

With optical microscopy (see Methods and Figure S14, Supporting Information), we investigated the electric field-induced domain switching in deformed $BaTiO_3$ single crystals, specifically from *a*-domains to *c*-domains. Initially, the deformed sample exhibited $a_1/a_2$ 90° stripe domains with domain walls parallel to the $[\bar{1}10]$ direction (**Figure 3**a). When an electric field of 2 kV $cm^{-1}$ was applied, the color contrast in the lower half of the sample began to blur, indicating the initiation of domain switching. At 4 kV $cm^{-1}$, this region completely switched to *c*-domains. As the electric field increased further, the domain walls merged, resulting in a single *c*-domain. After the electric field was removed, the domain structure exhibited partial recovery but did not fully revert to its initial state. Specifically, we observed the emergence of *a*/*c* 90° domain walls oriented at 135° with respect to the [110] direction. Figure 3b provides a two-dimensional X-ray diffraction (XRD) intensity map around $2\theta = 45°$, which reveals a shift of 0.554° in diffraction peaks from (200) to (002) as the electric field increases from 0 to 10 kV $cm^{-1}$ along [001] direction. This shift indicates a microscopic lattice strain change of 1.1%, reflecting the influence of the electric field on the crystal structure and the transition between *a*- and *c*-domains (i.e., {200} and {002} tetragonal Bragg peaks). In contrast, the macroscopic strain accounts for contributions from the overall piezoelectric response of the material and non-180° domain switching across the sample. The discrepancy between the microscopic and macroscopic strain values arises because the local and bulk strain responses are governed by

different mechanisms under the applied electric field. Notably, a critical field of 7 kV $cm^{-1}$ was marked by a dashed line, signifying the threshold at which significant domain switching occurred. Figure 3c presents XRD patterns under various electric fields. At 0 kV $cm^{-1}$, the deformed sample formed only *a*-domains. However, as the electric field increased, *c*-domains became more prominent. At 10 kV $cm^{-1}$, the sample predominantly consisted of *c*-domains. Upon removing the electric field, *c*-domains, mostly but not completely, switch back to *a*-domains, indicating an irreversible component to the domain switching process. Obviously, the degrees of domain switching in response to negative maximum electric fields are distinctly different, which inevitably results in the generation of substantial asymmetric strain (Figure 2b). Collectively, these optical images and XRD data illustrated the significant impact of the electric field on the structural properties of deformed $BaTiO_3$ single crystals. The observations highlighted the irreversible nature of the domain switching between *a*- and *c*-domains under different electric field conditions. Our previous results revealed that introducing dislocations with {110}<110> slip systems favored the formation of *a/c* domains in the unpoled state,[29] resulting in a reasonably reduced strain of 0.56% (Figure S15, Supporting Information). This reduction can be rationalized given that the pre-existing large amount of *c*-domains cannot be switched when an electric field was applied along the [001] direction. Therefore, our dislocation imprinting strategy offers a new dimension of control over microstructure and domain switching in ferroelectrics.

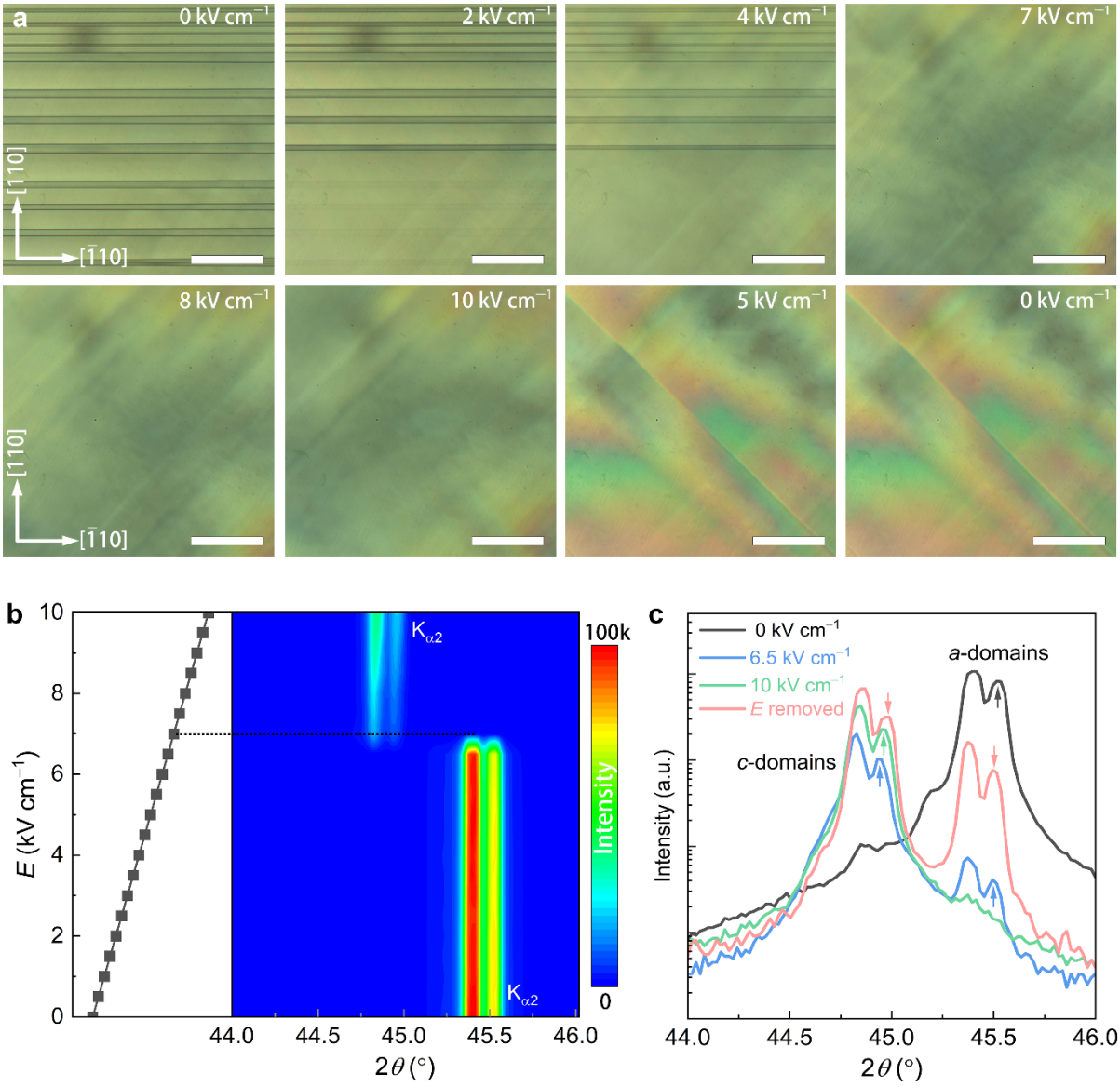


**Fig. 3**. a) Optical microscope images taken under different electric fields. Scale bar: 50 μm. b) Contour map of the (200) ($2\theta \approx 44.8°$) and (002) ($2\theta \approx 45.5°$) reflections. The left plot represents the electric evolution during the poling process. The panel c) highlights the (200) and (002) peaks under different electric fields. The positions of $K_{\alpha 2}$ reflections were marked by arrows.

To elucidate the role of introduced dislocations in the domain formation and domain switching of $BaTiO_3$, we performed three-dimensional phase-field simulations of bulk single-crystal $BaTiO_3$ with and without dislocation arrays to obtain the domain structure evolution under varied temperature and applied electrical and mechanical loads. The deformed $BaTiO_3$ is considered to be macroscopically stress-free but microscopically containing an array of edge dislocation pairs threading along [001], as displayed in Figure 4a and Figure S16 (Supporting

Information). We simulated the domain nucleation process by slowly cooling a paraelectric $BaTiO_3$ from 425 K (above the Curie temperature ($T_C$)) down to 300 K. After obtaining the equilibrium domain structure at 300 K, we applied a ramping electric field along [001] up to 30 kV $cm^{-1}$ (beyond the theoretical coercive field) to investigate the domain switching during poling. After removing the electric field, uniaxial compressive stress was applied along [001] to examine the domain switching by mechanical depoling. Details of the setup of the phase-field model for ferroelectrics with dislocations are given in the methods section.

We found that the introduced dislocations can serve as nucleation sites for the ferroelectric phase even at a temperature higher than $T_C$. The local stress field associated with the edge dislocations threading along [001] strongly favored the nucleation of domain variants with in-plane polarization components (i.e., $a_1^{\pm}$ and $a_2^{\pm}$) on opposite side of the glide plane of the dislocations, which is consistent with previous reports from phase-field simulations of $PbTiO_3$ thin films.[62,63] We also demonstrated that the charged state of dislocations is closely related to the nucleation and growth of 180° domains. For neutral dislocations, nucleation of alternating $a_1^+$ and $a_1^-$ and $a_2^+$ and $a_2^-$ domains separated by 180° domain walls along the dislocation lines is predominant, as featured in **Figure 4**a. The resulting equilibrium domain structure at 300 K consists of equivalent amount of $a_2^+$ and $a_2^-$ domains and needle-like $a_1^-$ domains emanating from the dislocation cores (Figure S17a and Video S1, Supporting Information). The nucleation of needle domains from the dislocation cores led to the pinning of domain walls, a phenomenon that was analyzed numerically.[64] In contrast, if the dislocation cores are charged, the associated local electric field can favor the nucleation of either variant of $a_1^-$ and $a_1^+$ (or $a_2^-$ and $a_2^+$), thereby suppressing the formation of 180° ferroelectric domain walls and resulting in columnar domains along the dislocation lines (Figure 4b). The equilibrium domain structure at 300 K consists of exclusively $a_2^+$ domains and needle-like $a_1^{\pm}$ domains, further detailed in Figure S17b and Video S2 (Supporting Information). The simulation helps to understand the mechanisms

behind the preferential formation of $a_1/a_2$ domains and the scarcity of 180° domain walls in the deformed samples in experiments. Our phase-field simulations revealed that $a_1/a_2$ domains of $BaTiO_3$ with charged dislocations can be irreversibly switched to a single *c* domain (Figure 4c,d) under an electric field above 2 kV $cm^{-1}$, giving rise to near 1.0% field-induced strains. The polarization vectors near dislocation cores become along [011] or [101] directions after poling. Furthermore, mechanical depoling by uniaxial compression is also demonstrated under 75 MPa loading through ferroelastic switching from *c* to $a_1/a_2$ domains (Figure 4e), aligning well with experimentally observed stress-associated domain switching (Figure 2e). Note that there are discrepancies between the calculated critical stress and electric field for domain switching and experimental values, stemming from the complexity of dislocation structures in the deformed samples that are more intricate than the simple dislocation arrays.

These findings underscore the potential of using plastic deformation to achieve preferential formation of domain variants. The substantial lattice distortion strain observed at the microscopic level could therefore translate macroscopically into a strain response determined by the tetragonality (*c*/*a*) of the single crystal. These insights into the role of dislocations in tailoring the microstructure and electrostrain properties of ferroelectric materials hold significant implications for the design and optimization of advanced actuator devices. Bridging the gap between dislocation engineering and practical applications, our study highlights the transformative potential for controlling domain structures in bulk ferroelectrics, potentially paving the way for functional materials with tailored electromechanical properties.

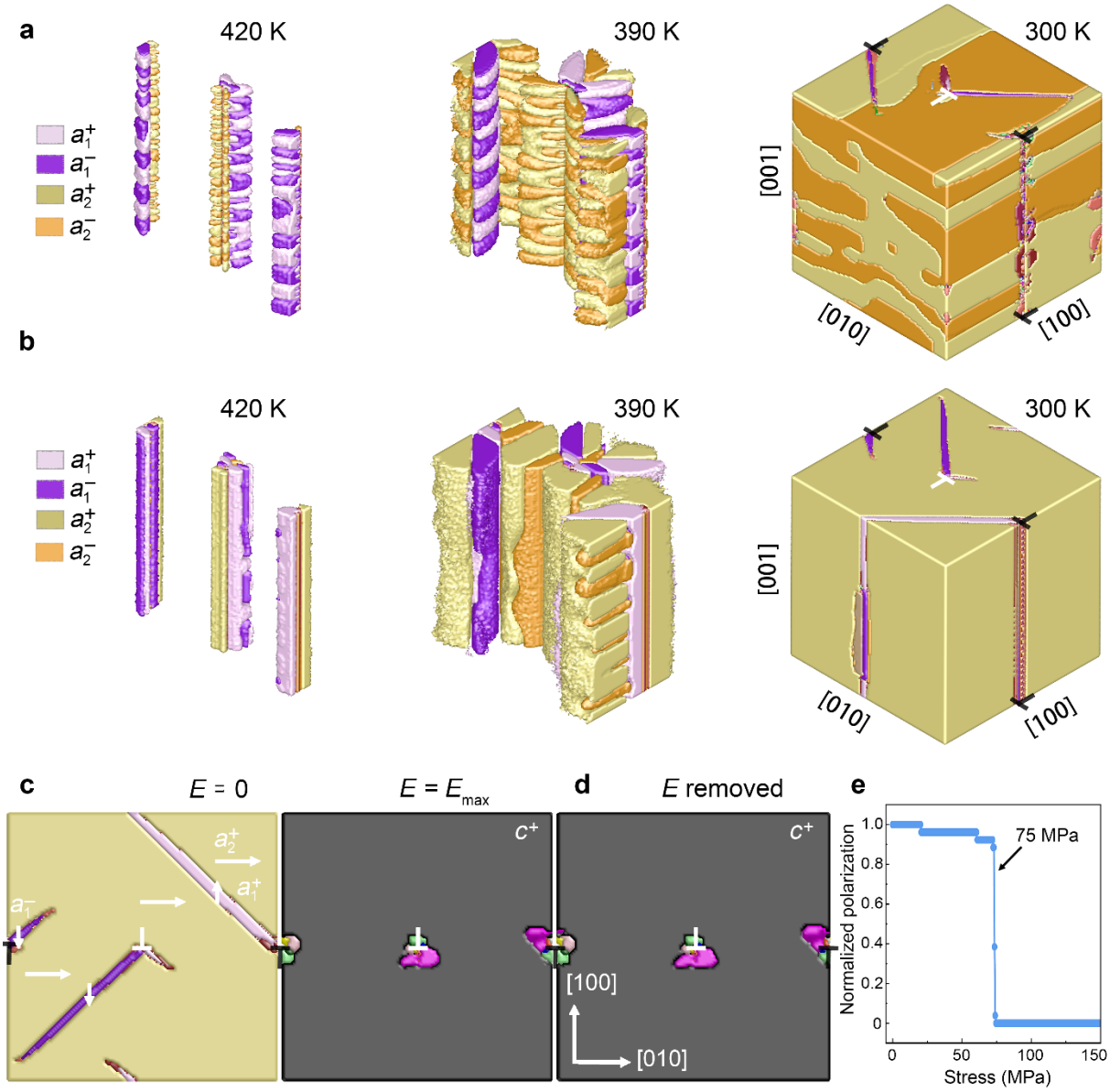


**Fig. 4.** Phase-field simulation results portray the mesoscale polarization distribution near a) uncharged and b) charged dislocation cores at selected temperatures during the cooling process from 420 K to 300 K under stress-free conditions. c) Phase-field simulation results exhibit the *a*-*c* domain switching triggered by the application of an electric field along the [001] direction. d) The domain structure post-removal of the applied electric field. e) Normalized polarization ($P/P_0$) as a function of uniaxial compressive stress, where $P_0$ represents the spontaneous polarization of the *c*-domains.

### 3. Conclusion

Our work demonstrated the potential of using charged dislocations as building blocks to tailor microstructures and tame macroscopic domain switching in bulk ferroelectrics. These dislocations, along with associated space charge layers, favorably nucleated ferroelectric

domains within the [100]/[010] plane. Through mechanical dislocation imprinting, we achieved a lock-in electrostrain of 0.69% along with an effective piezoelectric strain coefficient of 6900 pm $V^{-1}$. The above 1% reversible and irreversible electrostrains, approaching the limit of lattice distortion of 1.1%, can be fully unlocked by applying a compression stress of 6 MPa along the [001] direction, leading to an effective piezoelectric strain coefficient surpassing 10000 pm $V^{-1}$ and a record-high strain energy density of 11.67 J $cm^{-3}$. Both experimental and phase-field simulation results revealed that this exceptional electrostrain primarily results from the complete release of lattice distortion under applied electric field and mechanical stress, highlighting the potential of dislocation engineering in locking and unlocking the actuation performance of piezoelectric materials with simple chemical compositions. Besides ferroelectric ceramics, we anticipate that this mechanistic concept is also applicable to other ceramic systems, where dislocation technology can be employed to engineer microstructures with desired functionalities such as magneto-superelasticity,[65] thereby improving sustainability over chemical doping strategies.

## 4. Experimental Section

*High-temperature uniaxial compression*: [110]-oriented high-quality $BaTiO_3$ single crystals with dimensions of 4×4×8 $mm^3$ (Electro-Optics Technology GmbH, Germany) were subjected to a thermomechanical treatment, beginning with a gradual heating process to 1150 °C at a rate of 1 °C $min^{-1}$ while subjected to an uniaxial compressive pre-stress of 1.25 MPa along the [110] crystallographic direction. To ensure uniformity and stability, both temperature and mechanical stress were sustained for a duration of 30 min, allowing the crystals to attain thermal equilibrium. Subsequently, the crystals were subjected to uniaxial compression deformation at 1150 °C. This deformation process was performed using a load-frame (Z010, Zwick/Roell, Germany), meticulously outfitted with a linear variable differential transformer (LVDT) for precise displacement measurements. Employing a loading strain rate of $1.0 \times 10^{-5}$ $s^{-1}$ and unloading

force rate of 0.5 N $s^{-1}$, respectively, facilitated the activation of {100}<100> high-temperature slip systems within the crystal lattice.[28,66] This specific condition maximized the Schmid factor, indicative of a heightened propensity for dislocation slip along the (100) planes, thereby resulting in the generation of dislocations predominantly oriented along the [001] direction. After deformation, the crystals were slowly cooled to room temperature, maintaining a controlled cooling rate of 1 °C $min^{-1}$, all while retaining the uniaxial compressive stress of 1.25 MPa along the [110] crystallographic direction. By applying a stress much lower than the yield stress (~60 MPa at 1150°C), we ensured that the aligned dislocations introduced at 1150°C remained stable, and their behavior and distribution within the material were unaffected. The high-temperature creep experiment by loading along the [001] direction can be found in our previous report.[29] The dislocations in our samples were imprinted at 1150 °C. At lower temperatures (below 800 °C), these dislocations become completely immobile. As a result, there is no concern regarding long-term reliability, as dislocations are immobile on the glide plane used for imprint.

*Dislocation and domain structures*: Optical images of both reference and deformed $BaTiO_3$ single crystals were acquired using a LEXT OLS4100 laser scanning microscope (Olympus, Japan). To remove the additional dislocations introduced during cutting, the surfaces of sliced samples underwent polishing to achieve optical-grade quality using an automatic polisher (Phoenix 4000, Jean Wirtz GmbH, Germany). For *in situ* observation of the electric field-induced domain evolution, we utilized an Axio Imager2 microscope (Zeiss, Germany) equipped with a heating/cooling stage (HFS600E-PB4, Linkam Scientific Instruments, UK). The domain structures were captured employing both the differential interference contrast mode and reflection mode. Transparent gold electrodes were deposited onto both the top and bottom surfaces of the samples using a sputter coater EmiTech K950X (Quorum Technologies Ltd., UK). Voltages were applied using an electrometer (Model 6517, Keithley, USA).

To prepare the deformed crystals, they were sliced into 3×3 $mm^2$ square sheets with two large surfaces oriented along the [001] and [110] directions using a diamond saw (Model 4240, Well Diamantdrahtsägen GmbH, Germany). Subsequently, the specimen's thickness was mechanically reduced to 30 microns, followed by $Ar^+$ ion beam thinning (GATAN 695) to achieve the final thickness reduction after affixing the specimen with a copper ring (1.5 mm inner diameter). The as-polished samples were then annealed at 200 °C for 2 h (heating/cooling rate: 1 °C $min^{-1}$) to release the residual stresses generated from cutting and polishing. Bright-field TEM images were then obtained using a JEOL 2100F microscope (JEOL, Japan) operating at 200 kV. HAADF-STEM images were collected using a $C_s$-corrected JEM-ARM200F microscope (JEOL, Japan). The strain fields in HAADF-STEM images of deformed samples were extracted by GPA using the (100) and (010) reflections,[67,68] which was performed with Gatan Digital Micrograph software. The radius of the masks was selected as 1/2$a$ (100) of $BaTiO_3$. More details can be seen in Figure S3, Supporting Information.

Piezoresponse force microscopy (PFM) experiments were carried out at room temperature using a Cypher atomic force microscope (Asylum Research, USA) at a low scan rate of 0.5 Hz. PFM measurements were conducted employing conductive Cr/Pt-coated silicon cantilever tips with a spring constant of approximately 3 N $m^{-1}$ and a resonance frequency of about 75 kHz. A small AC driving voltage of 1 V (peak amplitude) was utilized during the overview PFM measurements. High-resolution PFM images were obtained in dual ac resonance tracking mode[69] by employing two drive frequencies near the tip-sample contact resonance frequency of approximately 350 kHz.

*Laboratory and synchrotron XRD*: Room temperature X-ray diffraction (XRD) patterns were collected using a custom-made diffractometer[70] featuring a RA-HF18 rotating anode source (Rigaku, Japan) operating at 50 kV and 300 mA. Doublet Cu $K_{\alpha1}$-$K_{\alpha2}$ radiation was utilized, with wavelength selection achieved via a graphite monochromator. The (002) peaks were collected within a 2$\theta$ range between 44° and 46° and steps of 0.02°. Each step had a counting

time of 2 s. Electric fields were applied using a Keithley model high voltage supply, ranging from 0 V to 700 V, with a step voltage of 35 V.

The deformed sample with optical-grade quality was further analyzed using scanning X-ray diffraction microscopy (SXDM) on the ID01 beamline at the European Synchrotron Radiation Facility. An incident X-ray energy of 9.5 keV was selected using a Si(111) double crystal monochromator with an energy resolution of $\Delta E/E = 10^{-4}$. A Fresnel zone plate with 300 µm diameter and 60 nm outer zone width was employed to focus the incident $10^{10}$ photons/sec into a spot of ~$60 \times 60 nm^2$, as measured by a ptychography scan of a known reference object. Diffraction patterns were collected using a 2D Si Maxipix detector placed 1.2 m downstream of the sample stage (see Figure S2, Supporting Information).[41]

Using the ID01 pseudo-six-circle diffractometer, the sample was placed at the 303 Bragg condition. This off-specular peak index was selected to obtain an incident beam angle close to 90°, minimizing the focused beam footprint and maximizing spatial resolution. A sample area of interest was chosen using an optical microscope mounted on the diffractometer. This area was then raster scanned along the sample in-plane axes relative to the focused beam in 80 nm steps over a $10 \times 10$ µm$^2$ area using a commercial piezoelectric stage. At each point of the raster, the area detector was exposed for 10 milliseconds, collecting a local 303 diffraction pattern. The motion of the piezoelectric stage and the detector readout are synchronized so that data collection occurs with no dead time. The raster scan was repeated at 60 different incident beam angles around the center of the 303 peak. After conversion from angular to orthonormal reciprocal space coordinates, the resulting SXDM dataset corresponds to an array of 3D-RSMs, one for each sample coordinate probed covered in the raster scan. Additional data processing allows to extract the distribution of the intensity and position of the 303 peak over the probed area, which in turn enables the computation of the local orientation of 303 planes relative to a reference.[71]

*Electrical measurements*: Gold electrodes were sputtered onto the two large top and bottom surfaces of the investigated samples with an electrode area of 4×4 $mm^2$ and a thickness of 1 mm to facilitate electrical measurements. Polarization hysteresis (*P*–*E*) and strain loops (*S*–*E*), as well as their temperature dependence were conducted at different frequencies utilizing a TF 2000E ferroelectric workstation (aixACCT Systems Inc., Germany) equipped with a temperature-controlled cell and a high-resolution double beam laser interferometer (SIOS Meβtechnik GmbH, Germany). The unipolar strains after multiple loadings, up to 100 cycles, were quantified at a frequency of 1 Hz with triangular voltage waveforms using the TF 2000E workstation. Polarization and strain loops under applied compressive stress were accurately quantified using a load frame (Z010, Zwick/Roell, Germany) equipped with a LVDT and a Sawyer-Tower setup. The voltage was amplified by a high-voltage amplifier (20/20C, TREK Inc., USA). To ensure precise strain measurements, the sample and the LVDT system were carefully aligned using a custom-built centering tool. This alignment minimized measurement errors and ensured accurate capture of strain data during the experiments. The sample displacement was measured using a single LVDT with a resolution of ±20 nm (W1ELA/0, HBM, Germany), comprising a core and coil assembly positioned below the sample (as shown in the inset of Fig. 2e). Compressive stress was applied along the [001] direction on samples with dimensions of 4×4×4 $mm^3$. The stability of unipolar strains under a compressive stress of 6 MPa was evaluated over 1000 cycles at a frequency of 1 Hz using the setup described above. Direct piezoelectric constant, $d_{33}$, and permittivity over time after poling (namely the aging experiment) were measured at room temperature employing a Berlincourt meter (PM300, Piezotest Pte. Ltd., Singapore). This setup applied a static clamping force of 2 N and a dynamic driving force of 0.25 N at a driving frequency of 110 Hz.

*Elastic modulus measurement*: The Young's modulus of the deformed sample was determined from the stress-strain curve obtained using a Z010 load-frame. A constant linear compression

rate of 0.1 N $s^{-1}$ was applied along the [001] direction during the measurement. The samples used for this test had dimensions of 4×4×4 $mm^3$.

*Phase-field simulations*: The phase-field method is employed to model the domain structure evolution in $BaTiO_3$ bulk single crystals as a function of temperature, applied electrical field and mechanical stress. The equilibrium domain structures are determined by evolving the spontaneous polarization, $\boldsymbol{P}$, using the time-dependent Ginzburg–Landau equation,

$$\frac{\partial \boldsymbol{P}}{\partial t} = -L\frac{\delta F}{\delta \boldsymbol{P}}. \quad (1)$$

The kinetic coefficient, $L$, is assumed to be isotropic. The total free energy of the ferroelectric material, $F$, comprises several components, including the bulk free energy density $f_{\text{bulk}}$, the electrostatic energy density $f_{\text{elec}}$, the elastic strain energy density $f_{\text{elas}}$, and the polarization gradient energy density $f_{\text{grad}}$, i.e., $F = \int_V f_{\text{bulk}} + f_{\text{elec}} + f_{\text{elas}} + f_{\text{grad}} dV$. The detailed expression of each energy density term has been documented in previous works[72,73] and the corresponding materials parameters of an eighth-order Landau-Ginzburg-Devonshire model of $BaTiO_3$ are given in Ref.[73]

During simulations, the system is assumed to maintain electrical and mechanical equilibrium at each time step. The total strain and stress are determined by solving the mechanical equilibrium equations subject to macroscopically zero stress conditions. The local mechanical stress stems from inhomogeneous non-elastic strains (i.e., eigenstrains) due to the electrostrictive effect $\varepsilon_{ij}^0 = Q_{ijkl}P_kP_l$ and the dislocations $\varepsilon_{ij}^{0,d}$. The eigenstrains of an edge dislocation with a Burger's vector $\boldsymbol{b}$ and glide plane normal vector $\boldsymbol{n}$ are described by:

$$\varepsilon_{ij}^{0,d} = \frac{b_i n_j + b_j n_i}{2d_0} \quad (2)$$

where $d_0$ is the spacing of the glide planes. The eigenstrains of dislocations are incorporated into the model in the reciprocal space following the method outlined by Ref.[74] To ensure the stress-free state of the system, an image edge dislocation with the opposite gliding plane normal direction is introduced at the periodic boundary of the simulation box (Figure S16).

The electric field is derived by solving the Poisson equation, $\nabla^2\phi = \frac{\rho}{\epsilon_0\epsilon_b}$, where $\rho$ represents the total charge density. The electrostatic potential $\phi$ is related to the electric field $E$ via $E = -\nabla\phi$. The vacuum permittivity $\epsilon_0 = 8.854\ \mathrm{N\ m^2\ C^{-2}}$ while the background relative dielectric constant $\epsilon_b$ is assumed to be 45. For modeling neutral dislocations, the only source of electric charges is the bound charges determined by the divergence of polarization vectors, $\rho_b = -\nabla \cdot \boldsymbol{P}$. For modeling charged dislocations, additional free charges are considered by introducing a disk of radius $r_c$ = 2 nm at the dislocation core with a uniform free charge density $\rho_f = 10^{22}$ electrons cm$^{-3}$. The total charge density is calculated as $\rho_t = \rho_f + \rho_b$. To ensure charge neutrality of the system, a disk carrying opposite charges with equal charge density is assigned to the core of the image dislocation. The time-dependent Ginzburg–Landau equation is iteratively solved using a semi-implicit Fourier spectral method.[75] The simulation system is discretized into a grid of $128\Delta x \times 128\Delta y \times 128\Delta z$ with grid size $\Delta x = \Delta y = \Delta z = 1$ nm. The periodic boundary conditions are adopted in all three dimensions.

**Supporting Information**

Supporting Information is available from the Wiley Online Library or from the author.

**Acknowledgements**

We thank Prof. Dragan Damjanovic for helpful discussions. We thank Prof. Karsten Durst for access to the laser scanning microscope, and Dr. C. Dietz and Prof. R. Stark for access to the Cypher atomic force microscope. We appreciate Phadcalc (www.phadcalc.com) for the excellent TEM service. Financial support by the German Research Foundation is gratefully acknowledged (project Nos. 414179371 and 530438323). The phase-field simulations and analysis were performed under the auspices of the National Science Foundation under DMR-2133373 (L.Q.C.) and under the U.S. Department of Energy by Lawrence Livermore National Laboratory under Contract DE-AC52-07NA27344 (B.W.). T.J. and L.M.-L. acknowledge the

European Research Council (ERC) "Horizon 2020" Program under Grant No. 805359-FOXON, Grant No. 957521-STARE and Grant No. 101088712-ELECTRON. The JEOL JEM-ARM200F TEM utilized in this study was partially funded by the German Research Foundation (DFG/INST163/2951). L.C. thanks the China Scholarship Council. L.C. and B.D. are grateful for the financial support from Agence Nationale de la Recherche (ANR) project RelaxTron (ANR-23-CE24-0011). B.D. acknowledges support from ANR through grant agreement ANR-23-CE09-0007 (SOFIANE). N.L. thanks the Guangxi Natural Science Fund for Distinguished Young Scholars (Grant No. 2022GXNSFFA035034). F.Z. acknowledges financial support from the Alexander von Humboldt Foundation (Grant No. 1203828) and the Ernst Ludwig Mobility Grant from the Association of Friends of Technical University of Darmstadt. The authors would like to thank the European Synchrotron Radiation Facility (ESRF) for provision of synchrotron radiation facilities for the beam time (Experiment session MA-6010) on beamline ID01.

**Conflict of Interest**

The authors declare no conflict of interest.

**Author Contributions**

F.Z. and B.W. contributed equally to this work. F.Z. and J.R. conceived the original idea. J.R. supervised the project. F.Z. and F.N. carried out deformation experiments, J.R., F.Z. and Y.L. discussed the deformation mechanisms. F.Z. and F.N. prepared the samples, together with N.L., L.F. and D.I., measured the electrical properties, and J.R., B.W., Y.L., L.F., N.L. and F.Z. contributed to the electrical data analysis. F.Z. and F.N. collected the optical and PFM images. P.B. designed the setup for *in-situ* optical observations. B.W. and L.-Q.C. performed the phase-field simulations. N.G. and C.L. collected the XRD data, together with B.D. supervised the analysis of the data. E.Z. conducted the SXDM experiments and analyzed the data. T.J. and

L.M.-L. performed the TEM experiments. F.Z. drafted the original manuscript with the inputs from all authors. All authors participated in discussions and commented on the paper.

**Data Availability Statement**

The data that support the findings of this study are available from the corresponding authors upon reasonable request. The SXDM dataset are available via doi.org/10.15151/ESRF-ES-1504506317.

Received: ((will be filled in by the editorial staff))
Revised: ((will be filled in by the editorial staff))
Published online: ((will be filled in by the editorial staff))

**References**

[1] B. Jaffe, W. R. Cook, H. Jaffe, *Piezoelectric Ceramics*, Academic Press, USA **1971**.

[2] J. Hao, W. Li, J. Zhai, H. Chen. *Mater. Sci. Eng. Rep.* **2019**, *135*, 1.

[3] K. Uchino, *Piezoelectric Actuators and Ultrasonic Motors*, Springer, USA **2011**.

[4] S.-E. Park, T. R. Shrout, *J. Appl. Phys.* **1997**, *82*, 1804.

[5] Y. Saito, H. Takao, T. Tani, T. Nonoyama, K. Takatori, T. Homma, T. Nagaya, M. Nakamura, *Nature* **2004**, *432*, 84.

[6] M. Acosta, N. Novak, V. Rojas, S. Patel, R. Vaish, J. Koruza, G. A. Rossetti, Jr., J. Rödel, *Appl. Phys. Rev.* **2017**, *4*, 041305.

[7] M. Waqar, H. Wu, J. Chen, K. Yao, J. Wang, *Adv. Mater.* **2022**, *34*, 2106845.

[8] W. Liu, X. Ren, *Phys. Rev. Lett.* **2009**, *103*, 257602.

[9] X. Gao, J. Yang, J. Wu, X. Xin, Z. Li, X. Yuan, X. Shen, S. Dong, *Adv. Mater. Technologies* **2020**, *5*, 1900716.

[10] K. Wang, J.-F. Li, *Adv. Funct. Mater.* **2010**, *20*, 1924.

[11] L. Peng, J. Zhai, B. Shen, S. Zhang, X. Li, F. Zhu, X. Zhang, *Adv. Mater.* **2018**, *30*, 1705171.

[12] H. Fu, R. E. Cohen, *Nature* **2000**, *403*, 281.

[13] D. Damjanovic, *Appl. Phys. Lett.* **2010**, *97*, 062906.

[14] M. Davis, D. Damjanovic, N. Setter, *Phys. Rev. B.* **2018**, *30*, 1705171.

[15] B. Wang, Y. Gu, S. Zhang, L.-Q. Chen, *Prog. Mater. Sci.* **2019**, *106*, 100570.

[16] F. Li, M. J. Cabral, B. Xu, Z. Cheng, E. C. Dickey, J. M. LeBeau, J. Wang, J. Luo, S. Taylor, W. Hackenberger, L. Bellaiche, Z. Xu, L.-Q. Chen, T. R. Shrout, S. Zhang, *Science* **2019**, *364*, 264.

[17] X. Ren, *Nat. Mater.* **2004**, *3*, 91.

[18] G. Huangfu, K. Zeng, B. Wang, J. Wang, Z. Fu, F. Xu, S. Zhang, H. Luo, D. Viehland, Y. Guo, *Science* **2022**, *378*, 1125.

[19] Y. Feng, J. Wu, Q. Chi, W. Li, Y. Yu, W. Fei, *Chem. Rev.* **2020**, *120*, 1710.

[20] D.-S. Park, M. Hadad, L. M. Riemer, R. Ignatans, D. Spirito, V. Esposito, V. Tileli, N. Gauquelin, D. Chezganov, D. Jannis, J. Verbeeck, S. Gorfman, N. Pryds, P. Muralt, D. Damjanovic, *Science* **2022**, *375*, 653.

[21] J. Wang, B. Wang, H. Zhang, S. Zhang, Y. Guo, *Adv. Mater.* **2024**, *36*, 2404682.

[22] X. He, M. A. Boda, C. Chen, R. Dun, L. Wang, Y. Bao, D. Pang, L. Guo, H. Zeng, Y. Li, Z. Yi, *Mater. Horiz.* **2024**, *11*, 1079.

[23] H. Luo, H. Liu, H. Huang, Y. Song, M. G. Tucker, Z. Sun,Y. Yao, B. Gao, Y. Ren, M. Tang, H. Qi, S. Deng, S. Zhang, J. Chen, *Sci. Adv.* **2023**, *9*, eade7078.

[24] W. Feng, B. Luo, S. Bian, E. Tian, Z. Zhang, A. Kursumovic, J. L. MacManus-Driscoll, X. Wang, L. Li, *Nat. Commun.* **2022**, *13*, 5086.

[25] S. Tian, B. Wang, B. Li, Y. Guo, S. Zhang, Y. Dai, *Sci. Adv.* **2024**, *10*, eadn2829.

[26] X. Fang, A. Nakamura, J. Rödel. *Am. Ceram. Soc. Bull.* **2023**, *102*, 24.

[27] M. Kissel, L. Porz, T. Frömling, A. Nakamura, J. Rödel, *Adv. Mater.* **2022**, *18*, 2001086.

[28] F. Zhuo, X. Zhou, S. Gao, F. Dietrich, P. B. Groszewicz, L. Fulanović, P. Breckner, B.-X. Xu, H.-J. Kleebe, D. Damjanovic, J. Rödel, *Phys. Rev. Lett*. **2023**, *131*, 016801.

[29] M. Höfling, X. Zhou, L. M. Riemer, E. Bruder, B. Liu, L. Zhou, P. B. Groszewicz, F. Zhuo, B.-X. Xu, K. Durst, X. Tan, D. Damjanovic, J. Koruza, J. Rödel, *Science* **2021**, *372*, 961.

[30] F. Zhuo, X. Zhou, S. Gao, M. Höfling, F. Dietrich, P. B. Groszewicz, L. Fulanović, P. Breckner, A. Wohninsland, B.-X. Xu, H.-J. Kleebe, X. Tan, J. Koruza, D. Damjanovic, J. Rödel, *Nat. Commun.* **2022**, *13*, 6676.

[31] F. Zhuo, X. Zhou, F. Dietrich, M. Soleimany, P. Breckner, P. B. Groszewicz, B.-X. Xu, G. Buntkowsky, J. Rödel, *Adv. Sci.* **2024**, *11*, 202403550.

[32] L. Molino, L. Aggarwal, V. Enaldiev, R. Plumadore, V. I. Fal´ko, A. Luican-Mayer, *Adv. Mater.* **2023**, *35*, 2207816.

[33] Q. K. Muhammad, L. Porz, A. Nakamura, K. Matsunaga, M. Rohnke, J. Janek, J. Rödel, T. Frömling, *Nano Energy* **2021**, *85*, 105944.

[34] D. Hull, D. J. Bacon, *Introduction to dislocations*. Butterworth-Heinemann, **2001**.

[35] A. Nakamura, K. Matsunaga, J. Tohma, T. Yamamoto, Y. Ikuhara, *Nat. Mater.* **2003**, *2*, 453.

[36] U. Messerschmidt, *Dislocation dynamics during plastic deformation*, Springer, Berlin, Heidelberg, Germany **2010**.

[37] Z. Zhang, W. Sigle, M. Rühle, *Phys. Rev. B* **2002**, *66*, 094108.

[38] Z. Dong, M. Huo, J. Li, J. Li, P. Li, H. Sun, L. Gu, Y. Lu, M. Wang, Y. Wang, Z. Chen, *Nat. Mater.* **2024**, *630*, 847.

[39] C. Richter, V. M. Kaganer, A. Even, A. Dussaigne, P. Ferret, F. Barbier, Y.-M. Le Vaillant, T. U. Schülli, *Phys. Rev. Appl.* **2022**, *18*, 064015.

[40] G. A.Chahine, M.-I. Richard, R. A. Homs-Regojo, T. N. Tran-Caliste, D. Carbone, V. L. R. Jaques, R. Grifone, P. Boesecke, J. Katzer, I. Costina, H. Djazouli, T. Schroederc, T. U. Schüllia, *J. Appl. Crystallogr.* **2014**, *47*, 762.

[41] S. J. Leake, G. A. Chahine, H. Djazouli, T. Zhou, C. Richter, J. Hilhorst, L. Petit, M.-I. Richard, C. Morawe, R. Barrett, L. Zhang, R. A. Homs-Regojo, V. Favre-Nicolin, P. Boesecke, T. U. Schüllia, *J. Synchrotron Radiat.* **2019**, *26*, 571.

[42] D. Damjanovic, *Rep. Prog. Phys.* **1998**, *61*, 1267.

[43] N. Balke, D. C. Lupascu, T. Granzow, J. Rödel, *J. Am. Ceram. Soc.* **2007**, *90*, 1081.

[44] W. J. Merz, *Phys. Rev.* **1949**, *76*, 1221.

[45] E. Burcsu, G. Ravichandran, K. Bhattacharya, *J. Mech. Phys. Solid.* **2004**, *52*, 823.

[46] J. Chen, J. E. Daniels, J. Jian, Z. Cheng, J. Cheng, J. Wang, Q. Gu, S. Zhang, *Acta Mater.* **2020**, *197*, 1.

[47] S.-T. Zhang, A. B. Kounga, E. Aulbach, H. Ehrenberg, J. Rödel, *Appl. Phys. Lett.* **2007**, *91*, 112906.

[48] X. Liu, X. Tan, *Adv. Mater.* **2016**, *28*, 574.

[49] Y. Wang, C. Luo, S. Wang, C. Chen, G. Yuan, H. Luo, D. Viehland, *Adv. Electron. Mater.* **2020**, *6*, 1900949.

[50] H. Zhang, C. Chen, H. Deng, B. Ren, X. Zhao, D. Lin, X. Li, H. Luo, *J. Mater. Chem. C* **2014**, *75*, 50.

[51] H. Zhang, H. Deng, C. Chen, L. Li, D. Lin, X. Li, X. Zhao, H. Luo, J. Yan, *Scripta Mater.* **2014**, *6*, 1900949.

[52] C. Hu, X. Meng, M.-H. Zhang, H. Tian, J. E. Daniels, P. Tan, F. Huang, L. Li, K. Wang, J.-F. Li, Q. Lu, W. Cao, Z. Zhou, *Sci. Adv.* **2020**, *6*, eaay5979.

[53] E. Sun, W. Cao, *Prog. Mater. Sci.* **2014**, *65*, 124.

[54] Y. Liu, Y. Zhou, H. Qin, T. Yang, X. Chen, L. Li, Z. Han, K. Wang, B. Zhang, W. Lu,

L.-Q. Chen, J. Bernholc, Q. Wang, *Nat. Mater.* **2023**, *22*, 873.

[55] H. Xu, Z.-Y. Cheng, D. Olson, T. Mai, Q. M. Zhang, G. Kavarnos, *Appl. Phys. Lett.* **2001**, *78*, 2360.

[56] Q. M. Zhang, V. Bharti, X. Zhao, *Science* **1998**, *280*, 2101.

[57] L. E. Cross, *Ceram. Trans.* **1996**, *68*, 15.

[58] V. Giurgiutiu, C. Rogers, *J. Intell. Mater. Syst. Struct.* **1996**, *7*, 656.

[59] F. Zhuo, U. R. Eckstein, N. H. Khansur, C. Dietz, D. Urushihara, T. Asaka, K.-i. Kakimoto, K. G. Webber, X. Fang, J. Rödel, *J. Am. Ceram. Soc.* **2022**, *105*, 4108.

[60] D. Torres-Torres1, A. Hurtado-Macias, R. Herrera-Basurto, E. Conteras, S. Sánchez, F. Mercader-Trejo, J. González-Hernández, O. Auciello, *J. Phys.: Condens. Matter* **2023**, *35*, 355703.

[61] Y. W. Li, F. X. Li, *Appl. Phys. Lett.* **2013**, *102*, 152905.

[62] S.Y. Hu, Y. L. Li, L. Q. Chen, *J. Appl. Phys.* **2003**, *94*, 2542.

[63] L. Cheng, H. Zhang, R. Xu, K. Co, N. Guiblin, M. Otoničar, C. Paillard, Y. Wang, B. Dkhil, *Appl. Phys. Lett.* **2023**, *123*, 201903.

[64] X. Zhou, Z. Liu, B.-X. Xu, *Inter. J. Solid. Struct.* **2022**, *238*, 111391.

[65] Q. Yu, J. Wang, C. Liang, J. Meng, J. Xu, Y. Liu, S. Zhao, X. Xi, C. Xi, M. Yang, C. Si, Y. He, D. Wang, C. Jiang, *Adv. Sci.* **2024**, *11*, 2401234.

[66] M. Höfling, L. Porz, M. Scherer, S. Gao, F. Zhuo, D. Isaia, J. Rödel, *J. Mater. Res.* **2022**, *37*, 737.

[67] M. J. Hÿtch, E. Snoeck, R. Kilaas, *Ultramicroscopy* **1998**, *74*, 131.

[68] M. J. Hÿtch, J.-L. Putaux, J.-M. Pénisson, *Nature* **2003**, *423*, 270.

[69] B. J. Rodriguez, C. Callahan, S. V. Kalinin, R. Proksch, *Nanotechnology* **2007**, *18*, 475504.

[70] J. F. Berar, G. Calvarin, D. Weigel, *J. Appl. Crystallography* **1980**, *13*, 201.

[71] I. Martens, N. Vostrov, M. Mirolo, S. J. Leake, E. Zatterin, X. Zhu, L. Wang, J. Drnec, M.-I. Richard, T. U. Schulli, *Nat. Commun.* **2023**, *14*, 6975

[72] L.-Q. Chen, *J. Am. Ceram. Soc.* **2008**, *91*, 1835.

[73] Y. L. Li, L. E. Cross, L. Q. Chen, *J. Appl. Phys.* **2005**, *98*, 064101.

[74] S.Y. Hu, L. Q. Chen, *Acta Mater.* **2001**, *49*, 463.

[75] L. Q. Chen, J. Shen, *Computer Phys. Commun.* **1998**, *108*, 147.

**We introduce a dislocation engineering strategy to unlock electrostrains and piezoelectric properties in lead-free $BaTiO_3$ single crystals, achieving a record-high strain energy density and large piezoelectric coefficient through domain structure design and controlled switching, with broad implications for advanced actuator applications.**

Fangping Zhuo, Bo Wang, Long Cheng, Edoardo Zatterin, Tianshu Jiang, Fan Ni, Patrick Breckner, Yan Li, Nicolas Guiblin, Daniel Isaia, Nengneng Luo, Lovro Fulanović, Leopoldo Molina-Luna, Brahim Dkhil, Long-Qing Chen, and Jürgen Rödel

**Unlocking electrostrain in plastically deformed barium titanate**